Richtmyer-Meshkov Instability in the Turbulent Regime

Guy Dimonte, C. Eric Frerking, and Marilyn Schneider
Lawrence Livermore National Laboratory, Livermore, California 94551
(Received 7 March 1995)

We investigate the Richtmyer-Meshkov instability in the turbulent regime with three-dimensional random interfacial perturbations. Experiments are conducted on the Nova laser with strong radiatively driven shocks (Mach > 20) in planar, two-fluid targets. The mixing zone at the interface is found to increase in time as $h \sim t^{\beta}$ with $\beta \sim 0.6 \pm 0.1$. Hydrodynamic simulations in 2D obtain similar values of h over the observation time, but with a larger exponent. A heuristic turbulent impulsive model is offered to identify the underlying processes.

PACS numbers: 52.35.Py, 52.35.Ra, 52.65.Kj

When a shock encounters a perturbed fluid discontinuity, the transmitted and reflected shocks are modulated, and they produce pressure variations in the upstream (1) and downstream (2) fluids that reinforce the initial interfacial perturbations and cause them to grow. This is the Richtmyer-Meshkov (RM) instability [1,2], and it occurs for fluids of different densities or compressibilities. In studies [1–9] with single sinusoidal perturbations, the measured growth rates have been reconciled with those calculated with full hydrodynamic simulations and linear impulsive models. As the perturbation grows to an amplitude comparable to its wavelength, the growth rate decreases and the amplitude saturates.

Single mode experiments provide insight and a fundamental test of theory, yet applications affected by hydrodynamic instabilities, such as inertial confinement fusion [10], involve perturbations which are three-dimensional (3D), random, and possibly turbulent. In the turbulent regime, the growth rate for the interfluid mixing zone h (peak-to-valley amplitude) differs from that in linear theory. For example, the Rayleigh-Taylor (RT) instability [11] transitions from exponential growth in the linear regime to $h \sim t^2$ in the turbulent regime [12]. The turbulent RM instability is predicted [13–15] to increase in time as $h \sim t^{\beta}$, with $1/3 < \beta < 1$. The RT scaling law has been determined experimentally, but the RM scaling law remains uncertain. We investigate the shock-induced (RM) growth of the turbulent mixing zone with 3D random perturbations and strong radiatively driven shocks. This extends previous investigations in shock tubes [6,16,17] to high compression, and we use experimental techniques that avoid membranes and edge effects.

We have conducted experiments on the Nova laser [18] at Lawrence Livermore National Laboratory which show that the mixing zone follows a power law with $\beta \sim 0.6 \pm 0.1$. Hydrodynamic simulations in 2D with a Lagrangian-Eulerian code [19] obtain comparable amplitudes, but the exponent is larger, $\beta \sim 0.9$. We formulate a heuristic impulsive model to identify the underlying processes, but 3D simulations [20] and more rigorous theoretical calculations are needed to explain the experimental results. Both are beyond the scope of this paper, since we estimate that a 3D simulation with radiation takes ~500 h of Cray YMP time.

The Nova experimental configuration has been described previously [3,4] and is shown in Fig. 1(a). In order to produce a spatially uniform drive, eight laser beams (28 kJ at 0.53 μm) are converted to soft x rays [18] inside a cylindrical radiation enclosure called a hohlraum (2500 μm diam, 3640 μm length). The laser beams enter the hohlraum through 1 mm diam holes at both ends in a 50° cone with respect to the x axis. A 3 ns long laser pulse generates a quasi Plankian [21] x-ray drive with a peak radiation temperature of 140 eV that lasts for ~4 ns. This generates a nearly constant velocity shock in a target mounted on a 740 μm hole in the hohlraum wall. The target is radiographed in-flight from the side using x rays generated by striking a vanadium foil (5.2 keV) with two independent laser beams of 5 ns duration. The gated x-ray imager (GXI) is a pinhole camera ($d = 10$ μm diam, 8× magnification) with a microchannel-plate detector (<0.1 ns gate). Fiducials provide absolute locations in z.

The target has two components, an ablator with density $\rho_1 \sim 1.65-1.85$ g/cm^3 and a foam tamper ($\rho^2 = 0.12$ g/cm^3). The Atwood number is $A = (\rho_2 - \rho_1)/(\rho_2 + \rho_1) \sim -0.86$. The shock originates in the ablator and couples to the tamper while exciting perturbations imposed at the ablator-tamper interface.

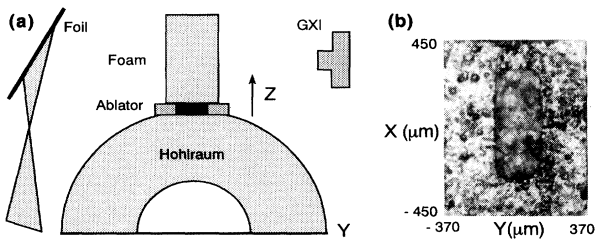

FIG. 1. (a) Schematic of target mounted on hohlraum with radiography configuration. (b) Photograph of interface of Be/Halar ablator. The scales in (a) and (b) are different as noted in the text.

0031-9007/95/74(24)/4855(4)$06.00

Although simple in principle, the target design is complex to facilitate the x-ray diagnosis. The peak-to-valley amplitude of the interfacial perturbations h is inferred from the spatial gradient of the ablator x-ray opacity at the interface. Since any tilt or curvature in the ablator can be mistaken for interfacial perturbations, we confine the radio-opaque material in the ablator to the center as shown in the face-on photograph in Fig. 1(b). The ablator consists of a 120 μm thick beryllium plate with a rectangular hole ($\delta y = 250$ μm, $\delta x = 600$ μm) in the center that is filled with Halar plastic ($C_4H_4F_3Cl$). The Halar is chosen because it is radio-opaque, yet its density (1.65 g/cm^3) is similar to that of the transparent Be (1.85 g/cm^3). Curvature and tilt effects are small over the $\delta y = \pm 125$ μm of the Halar tracer. Although not identical, the Be and Halar are similar hydrodynamically because their densities and atomic structures are similar. The Halar is pressed into the hole from the ablation front side using hot (130 °C) molds. The interface mold is sandblasted to obtain 3D random perturbations, whereas the ablation front mold is lapped flat. This process leaves a residual layer (<5 μm) of Halar on the Be on the ablation front side. The tamper consists of a low density foam (CHO) that has been machined to a block ($\delta y = 500$ μm, $\delta x = 900$ μm, and $\delta z = 900$ μm) and placed over the ablator as indicated in Fig. 1(a). The x-ray optical depth of compressed foam in y is $\tau \sim 0.4$, which is much smaller than $\tau \sim 5$ for Halar, but it is large enough to show the transmitted shock.

The imposed interfacial perturbations are characterized with a profilometer. Typical profiles and wave-number spectra are shown in Figs. 2(a) and 2(b) for the targets (solid lines) and the CALE simulations (dashed lines). The perturbations have an initial peak-to-valley amplitude of $h_0 \sim 16 \pm 3$ μm and a root-mean-squared (rms) initial amplitude of $\eta_{\rm rms} \sim 4.6 \pm 1$ μm. The spectral amplitude η_k in Fig. 2(b) is obtained by Fourier analyzing the profiles in x, but the perturbations are 3D and random in the experiment, whereas they are 2D and repetitive in CALE. Since the spectral phase space in multiple dimensions increases with wave number, we enhance the spectral amplitude in CALE at high k to compensate for its limited dimensionality. In addition, the Be has 10 μm wide, 2 μm deep pits, and the foam has 2–6 μm microcellular structures that are not represented in the experimental profile in Fig. 2. With broad spectra and $k\eta_k \ll 1$, the results are insensitive to the spectral details, and the instability starts in the linear regime and eventually becomes turbulent.

The shock-induced motion is obtained from side-on radiographs as shown in Figs. 3(a)–3(c) at $t =$ 0, 4.7, and 10.2 ns. The radiographs are analyzed using the respective x-ray transmission profiles $T_{\rm xr}(z)$ in Figs. 3(d)–3(f), which are taken near $x = 0$ to minimize curvature effects and averaged over $\delta x \sim 150$ μm to reduce noise. The minimum in $T_{\rm xr}(z)$ is ~5% rather than the expected 0.7% for Halar, and this is due to noise as determined by radiographing tungsten wires ($\tau \sim 50$). However, the ablation front (Ab), interface (I), and shock (S) are discernible. At $t = 0$, the target is free standing to exhibit the ablation front. At $t = 4.7$ ns, the target is compressed and the transmitted shock is just ahead of the interface. At 10.2 ns, the transmitted shock is well ahead of the interface and the shocked foam has $T_{\rm xr} \sim 0.6$ as expected. The interface and ablation front broaden in time. Although it is difficult to see in Fig. 3(c), the shock develops an 850 μm radius of curvature by 10.2 ns, which translates to an apparent width of only $\delta z \sim 9$ μm over the central $\delta x = \pm 125$ μm. From many measurements, we find that the incident shock

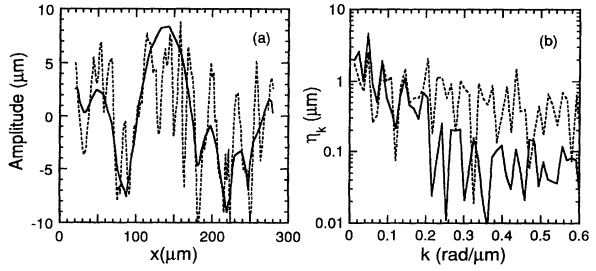

FIG. 2. Typical profiles of (a) initial perturbations and (b) Fourier spectra. Solid lines depict the experiment, and dashed lines represent the CALE simulations.

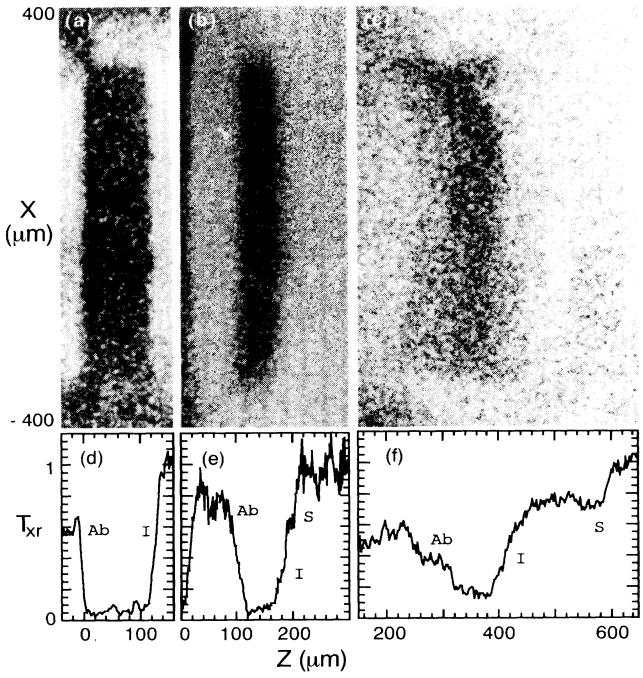

FIG. 3. Experimental side-on radiographs (a–c) and the respective spatial x-ray transmission profiles (d–f) at $t = 0$, 4.7, and 10.2 ns.

reaches the interface ($z = 120$ μm) at $t_i \sim 3.5-4$ ns, the transmitted shock has a velocity $V_2 \sim 70$ μm/ns, and the shock-induced interface speed is $U \sim 46$ μm/ns. From the axial compression in the radiographs, we estimate a postshock density of $\rho_1^* \sim 2$ g/cm^3 for the ablator and $\rho_2^* \sim 0.35$ g/cm^3 for the tamper. The postshock Atwood number is $A^* \sim -0.7$.

The perturbation amplitude is determined from the gradient of the x-ray transmission profiles at the interface. The peak-to-valley interfacial mixing zone is identified as $h \sim \Delta T_{xr}\ (dT_{xr}/dz)^{-1}$, where ΔT_{xr} and dT_{xr}/dz are the jump and gradient in the x-ray transmission at the interface, respectively. The technique is evaluated *in situ* by radiographing a 50 μm diameter tungsten wire and targets with known perturbations. The wire ($\tau \sim 50$) produces a minimum transmission of 5% ($\Delta T_{xr} \sim 95\%$), which is larger than expected and represents a noise baseline. In addition, the gradient length at the wire edge is $h \sim 10-12$ μm which is consistent with the 10 μm diameter GXI pinhole. The initial profile in Fig. 3(d) has a width of $h_{exp} \sim 19$ μm at the interface where $h_0 \sim 16$ μm and a smaller $h_{exp} \sim 13$ μm at the ablation front where $h_0 \sim 1-2$ μm. We remove the systematic instrumental broadening by subtracting the GXI pinhole diameter $d = 10$ μm in quadrature from the measured value h_{exp}. This yields $h \sim 16$ μm at the interface in agreement with profilometry, but it still overestimates the width of the ablation front by ~8 μm. This is a reasonable error estimate based on target tilt, curvature, and motion blurring. The profiles at 4.7 and 10.2 ns indicate a turbulent mix width of $h \sim 21$ and 75 μm, respectively.

The experiments are compared with 2D hydrodynamic simulations using the Lagrangian-Eulerian code CALE, which is driven with the measured radiation temperature profile [4]. The equations of state for Be and Halar are approximated with B_4C with density $\rho_1 = 1.65$ g/cm^3, and the foam is represented by CH with $\rho_2 \sim 0.12$ g/cm^3. The initial grid has 400 zones in z with 80 zones concentrated within ± 20 μm of the interface, and 130 zones covering 260 μm in x. With the single Plankian group radiation transport, a simulation to 15 ns takes ~10 h of CRAY YMP time. CALE obtains a peak pressure of 20 Mbar and average velocities $U \sim 46$ μm/ns and $V_2 \sim 70$ μm/ns similar to those measured. The incident shock velocity is $V_1 \sim 35$ μm/ns, which has not yet been measured. Simulated side-on radiographs and associated transmission profiles are shown in Fig. 4. The mix width increases to $h \sim 23$, 82, and 113 μm at 5, 10, and 15 ns. Although it is qualitative, bubble merger [13] is evident as the number of prominent features (amplitude $>0.7h$) declines from 12 to 8 to 4 in time. The ablation front is also distorted mainly at long wavelengths. The transmission profiles are monotonic at the interface, similar to those measured except for the plateau at 10 ns. This is not seen experimentally because the perturbations are 3D and the x rays propagate through an ensemble of spikes.

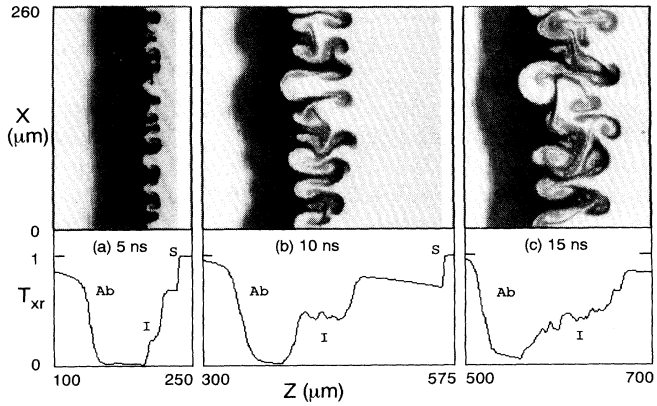

FIG. 4. Simulation side-on radiographs and spatial x-ray transmission profiles at $t = 0$, 5, and 10 ns.

Figure 5 shows the evolution of h for driven targets with $\eta_{rms} \sim 4.6$ μm. The points are experimental with the instrumental correction, and the solid line is from 2D CALE simulations. The perturbations are compressed ($\eta_0^*/\eta_0 \sim 1 - U/V_1 \sim -0.3$) with a phase reversal ($A < 0$) as the shock traverses the interface between 3 and 4 ns. The mix width then grows with comparable magnitudes in the experiment and simulations but at slightly different rates. To test self-similarity, we fit the power law $h \sim (t - t_i)^\beta$ to the experimental data and obtain $\beta \sim 0.6 \pm 0.1$. This agrees with the calculations [13] where $\beta \sim 0.4$ for bubbles and $\beta \sim 0.6$ for spikes at $IA^*I = 0.7$ (if they are symmetric in A^*, since only $0 < A^* < 1$ was considered). The CALE growth rate is nearly constant for $t < 10$ ns and then declines, implying an effective $\beta < 1$. This discrepancy may be due to small scale resolution limitations or that CALE is 2D instead of 3D. Clearly, further developments in simulations are required.

In addition to the displacement $U(t - t_i)$, a significant independent length scale is the initial amplitude h_0

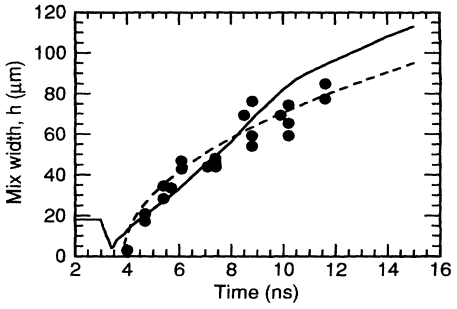

FIG. 5. The turbulent mix width at the interface vs time for the experiment (points), CALE (solid line), and Eq. (3) (dashed line) with $\eta_{rms} \sim 4.6$ μm, $h_{0e}^* = 5.6$ μm, and $t_i = 3.9$ ns.

(or feature size), and dimensional analysis implies that $h \sim [U(t - t_i)]^{\beta} h_0^{1-\beta}$. Indeed, in experiments and simulations with smaller h_0, we observe smaller mix widths consistent with $h \sim h_0^{1-\beta} \sim h_0^{0.4}$. This scaling law differs with that for RT turbulence where $h \sim t^2$ independent of initial conditions. This is reasonable since the acceleration is sustained in the RT case so that initial conditions can be forgotten, whereas in the RM case, the acceleration is impulsive and the initial conditions matter.

To identify a physical process that leads to an exponent $\beta < 1$, we offer the following heuristic model. From previous investigations [1–9], a single sinusoidal perturbation obeys

$$d\eta/dt \sim A^* k U \eta_{0e}^* . \tag{1}$$

The effective initial amplitude is $\eta_{0e}^* \sim (\eta_0^* + \eta_0)/2$ for $A < 0$ and $\eta_{0e}^* \sim \eta_0^*$ for $A > 0$ [1–5]. With a constant k, the amplitude grows linearly in time and eventually saturates [3,9] when the amplitude becomes large $k\eta \sim 1$. Thus, short wavelength modes grow quickly, but they saturate and will be overtaken by longer wavelength, slower growing modes. A broad spectrum of modes may be dominated by the just-saturated mode with $kI\eta I \sim \alpha_{\mathrm{RM}}$, where α_{RM} is an undetermined constant $O(1)$. This dynamic scale approximation simply quantifies the observation in simulations that the structure size increases with the mix width. With $k = \alpha_{\mathrm{RM}}/\eta$, $h = 2I\eta I$, and $h_{0e} = 2\eta_{0e}$, Eq. (1) becomes

$$dh^2/dt = 4\alpha_{\mathrm{RM}} I A^* U h_{0e}^* I \tag{2}$$

with a solution of

$$h = [h_{0e}^{*2} + 4\alpha_{\mathrm{RM}} I A^* h_{0e}^* I U(t - t_i)]^{1/2}. \tag{3}$$

The dashed line in Fig. 5 agrees with the data when $\alpha_{\mathrm{RM}} = 1.1$. We use $t_i = 3.9$ ns as the time the shock has traversed the interface, and $h_{0e}^* = 5.6$ μm. The exponent $\beta = 0.5$ is in line with our observations and bubble merger calculations [13]. With $\alpha_{\mathrm{RM}} = 1.1$, the dominant feature size is $k^{-1} \sim 0.45h$ consistent with the simulations. The RT turbulent scaling law can also be obtained with a dynamic scale approximation.

In conclusion, we studied the growth of the turbulent RM instability with 3D random initial interfacial perturbations and strong radiatively driven shocks. The turbulent mix width obeys $h \sim t^{\beta}$ with $\beta \sim 0.6 \pm 0.1$ consistent with bubble merger calculations. Our picture is that short wavelength modes grow quickly, but are overtaken by slower growing, longer wavelength modes. Hydrodynamic simulations in 2D obtain similar amplitudes but do not reproduce the temporal evolution in the experiment. We hope this stimulates more sophisticated turbulence calculations and 3D hydrodynamic simulations.

We are indebted to the fine Nova technical staff, R. Wallace and the target fabrication group, J. Ortel (LANL) for the GXI, and H. Kornblum for drive measurements. We thank Gene Burke and David Youngs for insightful conversations and M. J. Eckart for support. This work was performed under the auspices of the U.S. Department of Energy by the Lawrence Livermore National Laboratory under Contract No. W-7405-ENG-48.

[1] R. D. Richtmyer, Commun. Pure Appl. Math. **13**, 297 (1960).
[2] E. E. Meshkov, Izv. Akad. Nauk SSSR, Mekh. Zhidk. Gaza **4**, 151 (1969) [Izv. Acad. Sci. USSR Fluid Dynamics **4**, 101 (1969)].
[3] Guy Dimonte and Bruce Remington, Phys. Rev. Lett. **70**, 1806 (1993).
[4] Guy Dimonte *et al.* (to be published).
[5] K. A. Meyer and P. J. Blewett, Phys. Fluids **15**, 753 (1972).
[6] R. F. Benjamin, D. C. Besnard, and J. F. Haas, Los Alamos Report LA-UR 92-1185.
[7] L. D. Cloutman and M. F. Wehner, Phys. Fluids A **4**, 1821 (1992).
[8] J. W. Grove, R. Holmes, D. H. Sharp, Y. Yang, and Q. Zhang, Phys. Rev. Lett. **71**, 3473 (1993).
[9] A. N. Aleshin *et al.*, Sov. Tech. Phys. Lett. **14**, 466 (1988); A. N. Aleshin *et al.*, Sov. Phys. Dokl. **35**, 159 (1990).
[10] Recently reviewed by J. D. Kilkenny *et al.*, Phys. Plasmas **1**, 1379 (1994).
[11] Lord Rayleigh, *Scientific Papers II* (Cambridge, England, 1900), p. 200; Sir Geoffrey Taylor, Proc. R. Soc. London **A201**, 192 (1950).
[12] D. L. Youngs, Physica D **12**, 32 (1984); K. I. Read, Physica D **12**, 45 (1984).
[13] U. Alon *et al.*, Phys. Rev. Lett. **72**, 2867 (1994); **74**, 534 (1995).
[14] Serge Gauthier and Michel Bonnet, Phys. Fluids A **2**, 1685 (1990).
[15] K. O. Mikaelian, Physica D **36**, 343 (1989).
[16] V. A. Andronov *et al.*, Sov. Phys. JETP **44**, 424 (1976); V. A. Andronov *et al.*, Sov. Phys. Dokl. **27**, 393 (1982); S. G. Zaitsev *et al.*, Sov. Phys. Dokl. **30**, 579 (1985).
[17] M. Brouillette and B. Sturtevant, J. Fluid Mech. **263**, 271 (1994).
[18] Robert L. Kauffman *et al.*, Phys. Rev. Lett. **73**, 2320 (1994).
[19] R. Tipton (private communication). Radiation ALE codes are described in *Numerical Modelling in Applied Physics and Astrophysics,* edited by R. L. Bowers and J. R. Wilson (Jones and Barlett, Boston, 1991).
[20] D. L. Youngs, Phys. Fluids A **3**, 1312 (1991).
[21] H. N. Kornblum, R. L. Kauffman, and J. A. Smith, Rev. Sci. Instrum. **57**, 2179 (1986).

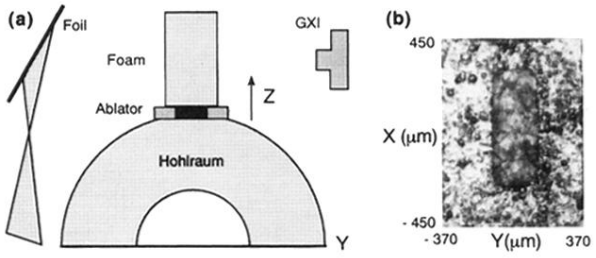

FIG. 1. (a) Schematic of target mounted on hohlraum with radiography configuration. (b) Photograph of interface of Be/Halar ablator. The scales in (a) and (b) are different as noted in the text.

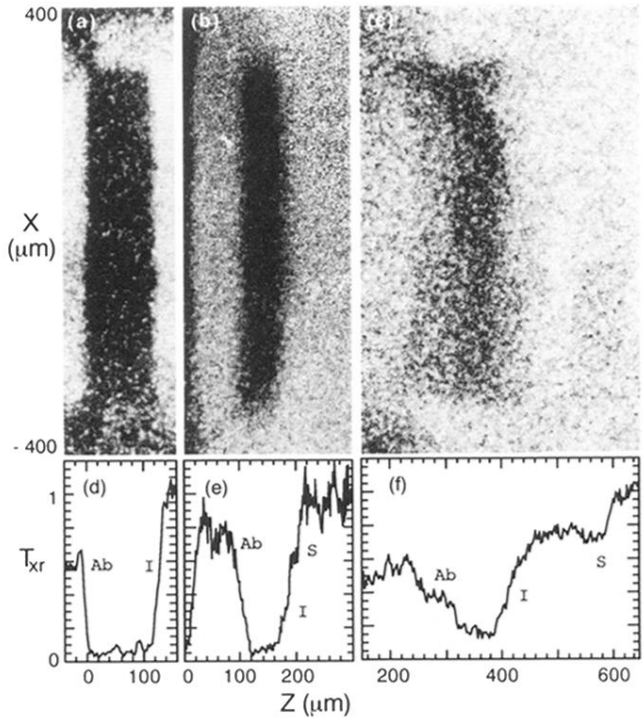

FIG. 3. Experimental side-on radiographs (a–c) and the respective spatial x-ray transmission profiles (d–f) at $t = 0$, 4.7, and 10.2 ns.

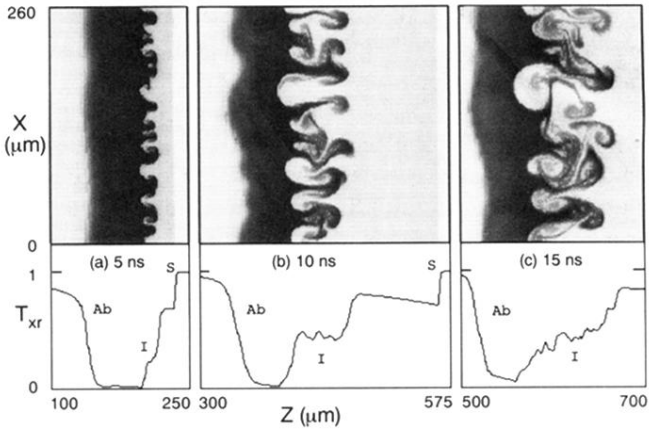

FIG. 4. Simulation side-on radiographs and spatial x-ray transmission profiles at $t = 0$, 5, and 10 ns.